

Simulating many-engine spacecraft: Exceeding 100 trillion grid points via information geometric regularization and the MFC flow solver

Benjamin Wilfong¹, Anand Radhakrishnan¹, Henry Le Berre¹, Nikolaos Tselepidis², Benedikt Dorschner², Reuben Budiardja³, Brian Cornille⁴, Stephen Abbott⁵, Florian Schäfer^{1,§}, Spencer H. Bryngelson^{1,§}

Abstract

This work proposes a method and optimized implementation for exascale simulations of high-speed compressible fluid flows, enabling the simulation of multi-engine rocket craft at an unprecedented scale. We significantly improve upon the state-of-the-art in terms of computational cost and memory footprint through a carefully crafted implementation of the recently proposed information geometric regularization, which eliminates the need for numerical shock capturing. Unified addressing on tightly coupled CPU–GPU platforms increases the total problem size with negligible performance hit. Despite linear stencil algorithms being memory-bound, we achieve wall clock times that are four times faster than optimized baseline numerics. This enables the execution of CFD simulations at more than 100 trillion grid points, surpassing the largest state-of-the-art publicly available simulations by an order of magnitude. Ideal weak scaling is demonstrated on OLCF Frontier and CSCS Alps using the full system, entailing 37.8K AMD MI250X GPUs (Frontier) or 9.2K NVIDIA GH200 superchips (Alps).

Keywords

computational fluid dynamics, gas dynamics, shock waves, extreme scale, unified memory

1 Introduction

The 21st century witnesses a “new space race”³⁰ driven by private companies replacing government agencies in providing launch services. The resulting drop in launch cost enabled a wide range of business models, ranging from satellites to space manufacturing^{2,14}. The new emphasis on scale and cost efficiency motivated innovations in rocket design, most notably the reuse of rocket stages and the leveraging of economies of scale.

An example of innovations motivated by industrial space exploration is the use of rockets with many engines. Five large F-1 engines powered the first stage of the Saturn V rocket. The width of the 3.7 by 5.6 meter F-1 engines was not constrained by road width or transportation logistics but primarily dictated by engineering requirements, such as thrust production, fuel flow rates, and structural integrity. As a result, they were transported using specialized equipment, including barges and oversized transport vehicles. Instead, SpaceX Super Heavy, the first stage of Starship, is powered by 33 smaller Raptor engines. This has multiple advantages. The economy of scale benefits the production of a larger number of smaller engines. The Raptor engine’s relatively compact size, with a nozzle diameter of approximately 1.3 meters (4.3 feet), allows it to be transported via standard road infrastructure. The multitude of engines also provides a degree of redundancy, allowing a small number of engine failures to be compensated for without compromising mission success. Upon reuse, the defective engines can be replaced. Further, when landing the Super Heavy after

flight, thrust can be reduced by turning off individual engines.

For all their advantages, using large arrays of small engines creates new design challenges. When closely packed, large numbers of engines can interact with their exhaust plumes, propelling hot gas upward toward the rocket’s base, thereby heating it. This so-called base heating can lead to mission failure²⁹, mandating the installation of heat shields on the rocket base. This requires heavier or more expensive materials for the base, motivating the search for a targeted design.

Mitigating base-heating problems most cost-efficiently, in terms of both dollars and weight, requires appreciating the mechanism by which engine exhaust is reflected back to the rocket and which parts of the rocket are most affected. A key difficulty in experimental approaches to understanding plume recirculation is that it depends on numerous parameters, including varying ambient pressure as the rocket traverses the atmosphere

¹Georgia Institute of Technology, Atlanta, GA, USA

²NVIDIA Corporation

³Oak Ridge National Laboratory, Oak Ridge, TN, USA

⁴Advanced Micro Devices, Inc.

⁵Hewlett Packard Enterprise

[§]Equal contribution

Corresponding author:

Spencer H. Bryngelson, Georgia Institute of Technology, Atlanta, GA USA 30332

Code availability: <https://github.com/MFlowCode/MFC>

Email: shb@gatech.edu

and engine thrust vectoring for steering. Numerical simulations are the only feasible means of obtaining a detailed characterization of the entire flow field under a broad range of conditions. They even allow probing the impacts of changes to the rocket design. Prior work on the numerical simulation of interacting rocket plumes was limited to small numbers (up to 7) of rocket engines and limited resolution (up to ≈ 10 million grid points)^{29,33,42,43}. Our work addresses this limitation via the latest flagship exascale systems, leveraging their hardware design and coupling novel algorithms, computational methods, and the optimizations they enable. With this, we can simulate the interaction of rocket engine plumes at unprecedented scales.

In this work, we **1.** use information geometric regularization to forego nonlinear viscous shock capturing, enabling the use of linear numerics with drastically reduced memory footprint. **2.** use unified addressing on tightly coupled CPU–GPU platforms to increase the total problem size with negligible performance hit. **3.** show that our approach is up to 5.7 times as energy efficient as an optimized implementation of state-of-the-art nonlinear numerical methods (WENO+HLLC), measured in the same codebase. **4.** improve the time to solution by a factor of 4. **5.** achieve the first, to the authors’ knowledge, public-domain CFD simulation of over 100 trillion grid points, exceeding the largest previous compressible simulation by an order of magnitude and the largest previous incompressible simulation by a factor of 3.5.

The model equations solved in this work are outlined in section 2. Related work and state-of-the-art methodologies are reviewed in section 3. Our strategy for enabling large-scale, high-fidelity simulations is detailed in section 4. The flagship computers used for this study are introduced in section 5. Results on performance and energy usage are presented in section 6, while simulation outcomes are discussed in section 7. Finally, a summary of the work is provided in section 8.

2 Physical model equations

As a model, we represent the exhaust via compressible Navier–Stokes equations

$$\frac{\partial \rho}{\partial t} + \nabla \cdot (\rho \mathbf{u}) = 0, \quad (1)$$

$$\frac{\partial (\rho \mathbf{u})}{\partial t} + \nabla \cdot (\rho \mathbf{u} \otimes \mathbf{u} + p \mathbf{I} - \boldsymbol{\tau}) = \mathbf{0}, \quad (2)$$

$$\frac{\partial E}{\partial t} + \nabla \cdot [(E + p) \mathbf{u} - \mathbf{u} \cdot \boldsymbol{\tau}] = 0, \quad (3)$$

with the ideal gas law equation of state

$$p = (\gamma - 1) \rho e, \quad \text{for } e := E/\rho - \|\mathbf{u}\|^2/2. \quad (4)$$

We denote as μ and ζ the shear and bulk viscosity, and use the constitutive law

$$\tau_{ij} = \mu \left(\frac{\partial u_i}{\partial x_j} + \frac{\partial u_j}{\partial x_i} \right) + (\zeta - 2\mu/3) \delta_{ij} \frac{\partial u_i}{\partial x_j}. \quad (5)$$

Equations (1) to (3) describe the conservation of mass, momentum, and energy, $\boldsymbol{\tau}$ is the viscous stress tensor,

and p is the pressure. Tracking mixture ratios of different gases/fluids and their chemical reactions would be a natural extension, though they are not necessary for this work. For the purpose of demonstrating our solution, we focus on eqs. (1) to (5).

3 Challenges and existing solutions

3.1 Shock capturing

3.1.1 Shock waves are the dominant concern in the simulation of high-speed compressible fluid dynamics. They arise in numerous natural and man-made phenomena, including supernovae, air, and spacecraft. The velocity and density fields of compressible high-speed flows sharpen over time, eventually forming macroscopic discontinuities or shock waves. However, on the microscopic scale, the gas viscosity balances the steepening of shock waves, resulting in smooth profiles. In practice, this happens on the scale of the mean free path of gas particles, orders of magnitude smaller than the scale of typical quantities of interest.

3.1.2 Computation with shocks: A multiscale problem. Higher-order numerical methods exploit the target solution’s regularity to approximate it with smooth functions, most frequently polynomials. The mean-free path is many orders of magnitude shorter than a realistic computational grid spacing. Thus, shocks appear as discontinuities on the grid scale, and the direct application of higher-order methods leads to Gibbs–Runge oscillations and subsequent simulation failure. *Shock capturing* modifies either the equation or its discretization to obtain an object that is well-behaved on the grid scale. It amounts to coarse-graining the microscopic shock and correctly representing its macroscopic effects without grid-resolving it. Crucially, the resulting coarse-scale model should preserve smooth grid-scale oscillations due to turbulence, reactions, or acoustic effects.

3.1.3 Existing approaches. Artificial viscosity mitigates Gibbs–Runge oscillations at the cost of excessive dissipation of fine-scale features. To remedy the latter, numerous approaches apply artificial diffusivity *adaptively*, in the vicinity of the shock^{3,4,12,18,19,23,28,31}. This is challenging in practice: A lack of viscosity creates spurious oscillations, while excessive viscosity dissipates the solution. Common choices, such as the localized artificial diffusivity of Cook and Cabot¹², struggle with three main challenges (fig. 2). First, while they allow spreading the shock over multiple grid points, the resulting shock profile is not smooth to higher order. In practice, this can lead to Gibbs–Runge oscillations overcoming the artificial viscosity, resulting in a breakdown of the simulation. Second, increasing the width of the shock requires increasing the strength of the artificial viscosity, which smears true physical features that are critical to representing the flow field, such as turbulent eddies. Lastly, in the presence of sufficiently strong shocks, the required artificial viscosity affects the CFL numbers of the explicit time steppers considered state-of-the-art for

such hyperbolic problems. Limiters are an alternative to artificial viscosity. They adaptively lower the order of the numerical method near shocks^{21,24,27,36,38,41}. They are more robust but also risk dissipating fine-scale features. Riemann solvers attempt to mitigate this problem, at additional computational cost^{22,34,39,40}.

3.2 GPU memory

The evolution of GPU memory over the past decades, in terms of capacity and bandwidth, has been highly beneficial for the memory-bound computation typical for CFD applications. The spatio-temporal scale separation in fluid flows requires a high resolution, which necessitates large amounts of memory that must be accessed at high speeds. Both NVIDIA and AMD have blurred the lines between GPU and CPU memory by introducing coherent CPU-to-GPU interfaces, 900 GB/s for the NVIDIA Grace-Hopper superchip. At the same time, AMD has implemented InfinityFabric at 8x36 GB/s for the AMD Trento+4 MI250X in the HPE Cray EX255a. These fast interconnects, along with technologies such as NVIDIA’s unified virtual memory (UVM), allow the use of CPU memory for GPU computations and even (in the case of Grace-Hopper) allow the GPU to saturate the host memory bandwidth.

3.3 Floating point computation

The advent of artificial intelligence and machine learning has fueled the development of algorithms with reduced and mixed precision. Yet, their adoption in HPC applications remains limited. The majority of traditional scientific applications to date rely on FP64 computation and storage. FP64 is the current standard for solving compressible, shock-laden flows. However, recent advances in software, hardware, and algorithms demonstrate great potential, as shown, for instance, in the iterative refinement of solving linear systems (see, e.g., Dongarra et al.¹⁵, Haidar et al.²⁰ or the HPL-MxP benchmark²⁵). We show that lower precision storage is viable for this work’s regularized flow model.

3.4 The need for scale

Current CFD simulations struggle to resolve phenomena across vastly different space and time scales. Fluid dynamics inherently involves multiscale interactions, such as large coherent structures and small turbulent eddies. Ultra-large simulations can broadly extend current scientific capabilities. In this case of this work, expanding from the current state-of-the-art ≈ 1 trillion grid points to *100 trillion* enables scale-resolved flow features of rocket exhaust.

For external aerodynamics, such as the jets we focus on in this study, the interaction between large-scale wake structures and small vortices is crucial for high-fidelity predictions. Current methods force compromises. Large simulations are required to represent shock waves, acoustic phenomena, and their turbulent interactions. Current state-of-the-art methods suffer from numerical dissipation, smearing critical flow features. By combining high resolution with low

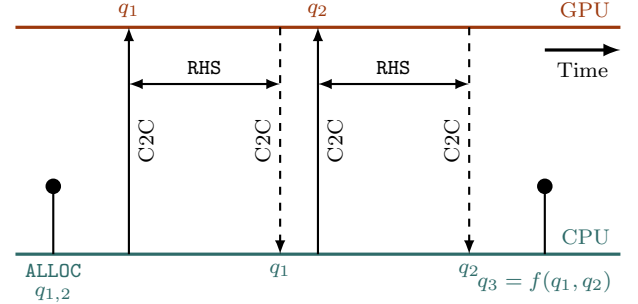


Figure 1. Schematic of the chip-to-chip (C2C) transfers of intermediate time-step variables between the on-node CPU and GPU devices. The time sub-steps are $q_{1,2}$ and the full step integration is q_3 .

walltime cost per grid point and leveraging an *inviscid* regularization (IGR), we reduce cell sizes relative to flow feature scales, thereby overcoming these challenges.

Large-scale CFD simulations have progressed from CPU-based runs, such as the 10T grid point simulation on IBM BlueGene/Q³⁵, which benefited from large CPU memory but was limited by slow processing speeds, to recent GPU-based efforts where compressible problems of similar scale have been solved on systems like OLCF Frontier³⁷. The largest GPU simulations for incompressible flows now reach approximately 34T grid points⁴⁵, though their performance relies on costly all-to-all communication. Lattice Boltzmann methods, suitable for near-incompressible flows and run in FP16, could reach 25T lattice points on Frontier (not demonstrated), albeit with lower accuracy compared to high-order accurate CFD methods²⁶.

4 Computational Methodology

4.1 Shock treatment with information geometric regularization

4.1.1 Information geometric regularization. We overcome the limitations of conventional approaches to shock capturing by utilizing the inviscid *information geometric regularization* recently proposed by Cao and Schäfer⁸. Cao and Schäfer⁸ first derive IGR in the pressureless (infinite Mach number) case, where shocks amount to a loss of injectivity of the flow map $x \mapsto \phi_t(x)$ that maps gas particles from their initial position to their position at time t . They modify the geometry according to which the flow map evolves, such that particle trajectories $t \mapsto \phi_t(x_0)$ never cross but instead approach each other asymptotically as shown in fig. 3. It preserves the nominal long-time behavior of solutions while avoiding the formation of singularities, recovering the nominal vanishing viscosity solutions in the limit. In the unidimensional, pressureless case, Cao and Schäfer⁹ proves this result rigorously. The modified geometry on flow maps arises from the information geometry of the mass density¹, accounting for its meaning as a probabilistic density estimate of particle positions. Cao and Schäfer⁸ refers to this perspective as *information geometric mechanics*.

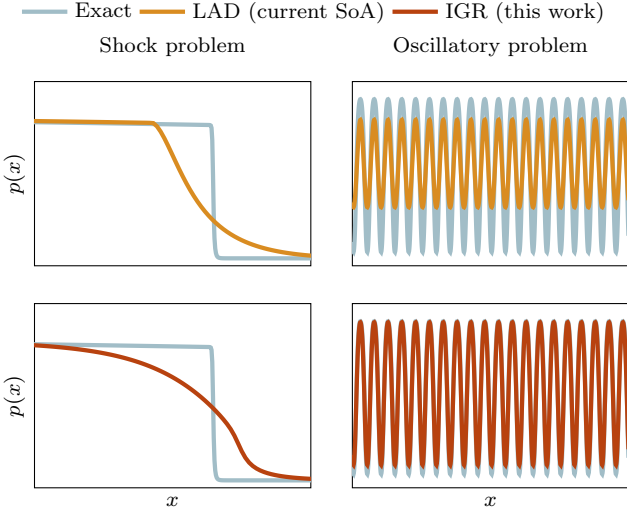


Figure 2. Inviscid regularization. Localized artificial diffusion (LAD) spreads shocks over a user-defined width (top left). SoA indicates state-of-the-art. The resulting profile is not a high-order smooth curve. Furthermore, increasing the width to account for coarser discretizations yields the physically meaningful dissipation of oscillatory solutions (top right). Information geometric regularization replaces shocks with smooth profiles at the grid scale and preserves oscillatory features (bottom row).

Following Cao and Schäfer⁸, IGR for the compressible Euler equations is obtained by adding the so-called *entropic pressure* Σ to p , resulting in the modified conservation law:

$$\frac{\partial \rho}{\partial t} + \nabla \cdot (\rho \mathbf{u}) = 0, \quad (6)$$

$$\frac{\partial (\rho \mathbf{u})}{\partial t} + \nabla \cdot (\rho \mathbf{u} \otimes \mathbf{u} + (p + \Sigma) \mathbf{I} - \boldsymbol{\tau}) = \mathbf{0}, \quad (7)$$

$$\frac{\partial E}{\partial t} + \nabla \cdot [(E + p + \Sigma) \mathbf{u} - \mathbf{u} \cdot \boldsymbol{\tau}] = 0, \quad (8)$$

$$\alpha (\text{tr}(\nabla \mathbf{u})^2 + \text{tr}^2(\nabla \mathbf{u})) = \frac{\Sigma}{\rho} - \alpha \nabla \cdot \left(\frac{\Sigma}{\rho} \right). \quad (9)$$

As shown in fig. 2, this *inviscid regularization* yields smooth solutions without damping fine-scale features. The parameter α determines the width of the smoothly expanded shocks, which is on the order of $\sqrt{\alpha}$. Computing the flux requires solving the auxiliary elliptic eq. (9), but $\sqrt{\alpha}$ is proportional to the mesh size. Hence, the resulting discrete system is uniformly well-conditioned and grid-point-local. With the previous solution as a warm start, $\lesssim 10$ Jacobi sweeps per flux computation suffice at negligible computational cost.

4.1.2 Discretization. IGR enables us to bypass shock capturing and instead employ a fifth-order accurate finite volume method with Lax–Friedrichs numerical fluxes for the hyperbolic part of the equation. Due to the high Reynolds number of the problem under consideration, we find that a second-order accurate approximation of the derivatives of \mathbf{u} suffices to compute the viscous stress tensor. We reuse the same derivatives to compute the left-hand side of eq. (9) and discretize

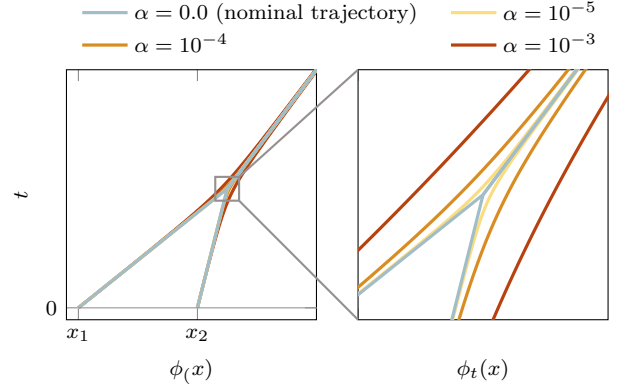


Figure 3. Information geometric regularization regularizes shocks by changing the geometry according to which the flow map ϕ_t evolves in time. When tracing two particles x_1 and x_2 , we see that in the modified geometry, their trajectories $t \mapsto \phi_t(x_1), \phi_t(x_2)$ no longer cross but instead converge asymptotically. The rate of convergence is determined by the parameter α modulating the strength of the regularization. The limit $\alpha \rightarrow 0$ recovers the nominal vanishing viscosity solution of the problem. Figure reproduced from Cao and Schäfer⁸, with author permission.

the elliptic operator on the right using a standard 6-point stencil. For each computation of the hyperbolic flux, we solve eq. (9) using up to ten sweeps of Jacobi iteration, with the previously computed Σ as an initial guess. Following Coralic and Colonius¹³, we use a third-order accurate Runge–Kutta method for time stepping¹⁷. For a single fluid case, the total number of floating point numbers stored by our scheme is $13N + o(N)$, where $o(N)$ is the number of grid points. This includes 5 arrays for the solution (density, energy, and three momenta), 5 arrays for the intermediate Runge–Kutta step, one array for Σ , one for the left-hand side of eq. (9), and one that serves as intermediate storage holding derivative reconstructions.

4.2 The algorithm

The key algorithmic kernel of our method computes the right-hand side of the ordinary differential equation obtained from the spatial discretization. It is presented in algorithm 1. We advance the conservative variables (line 1) at the cell centers using a 3rd-order accurate Runge–Kutta time stepper, which requires 2 copies of state variable buffers. The flux calculations at the cell boundaries are split dimensionally across the three coordinate directions (line 12). The conservative variables are reconstructed at the cell boundaries using a 5th-order accurate polynomial interpolation scheme (lines 23 to 28). In addition, the viscous fluxes require the calculation and reconstruction of velocity gradients (lines 16 to 18). A conversion of the reconstructed conservative variables to their primitive form is performed at the cell boundaries (lines 25 and 29). The Riemann problem at the interface is then solved using a Lax–Friedrichs approximate Riemann solver (lines 26 and 34). The net flux at the cell center is an input to the time stepper (line 4) via the right-hand side. The entropic pressure Σ is calculated at

Algorithm 1: Compute right-hand side (RHS)

```

1   $(\rho, \rho\mathbf{u}, E, \alpha) \leftarrow$  Conservative variables
2   $(\mathbf{u}, p) \leftarrow$  Primitive variables
3   $\Sigma \leftarrow$  Entropic pressure
4   $\text{rhs} \leftarrow$  Time stepper RHS
5   $\text{vflux} \leftarrow$  Temp. array for viscous flux
6   $\text{coeff} \leftarrow$  Reconstruction coefficients
7   $\text{igr\_rhs} \leftarrow$  RHS for elliptic solve
8   $\text{igr\_func}() \leftarrow$  Routine to calculate  $\text{igr\_rhs}$ 
9   $\text{viscous}() \leftarrow$  Routine for viscous flux
10  $\text{flux}() \leftarrow$  Routine for inviscid flux
11 for  $t = 1$  to  $T$  do // Loop over time steps
12   for  $\text{idir} \leftarrow (x, y, z)$  do // Loop over domain
13     foreach  $(i, j, k)$  in cells do
14       for  $q \leftarrow -2, 3$  do // Reconstruction
15         for  $n \leftarrow (x, y, z)$  do
16           compute  $\frac{du}{dn}$ 
17            $\text{vflux}_L \leftarrow \text{vflux}_L + \text{coeff}_L(q) \cdot \frac{du}{dn}$ 
18            $\text{vflux}_R \leftarrow \text{vflux}_R + \text{coeff}_R(q) \cdot \frac{du}{dn}$ 
19           if  $\text{idir} == x \ \&\& \ q == 0$  then
20             store  $\frac{du}{dn}$ 
21         if  $\text{idir} == x \ \&\& \ q == 0$  then
22            $\text{igr\_rhs} \leftarrow \text{igr\_func}(\frac{du}{dx} \frac{du}{dy} \frac{du}{dz})$ 
23           // Recon. density, velocity
24            $\rho_L, \rho_R \leftarrow \rho(-2 : 3)$  along  $\text{idir}$ 
25            $\rho\mathbf{u}_L, \rho\mathbf{u}_R \leftarrow \rho\mathbf{u}(-2 : 3)$  along  $\text{idir}$ 
26           // Convert to primitive
27            $\mathbf{u}_L, \mathbf{u}_R \leftarrow \rho\mathbf{u}_L, \rho\mathbf{u}_R$ 
28           // Viscous fluxes
29            $\text{rhs} \leftarrow \text{viscous}(\text{vflux}_L, \text{vflux}_R, \mathbf{u}_L, \mathbf{u}_R)$ 
30           // Recon. remaining variables
31            $E_L, E_R \leftarrow E(-2 : 3)$  along  $\text{idir}$ 
32            $\alpha_L, \alpha_R \leftarrow \alpha(-2 : 3)$  along  $\text{idir}$ 
33           // Convert to primitive
34            $p_L, p_R \leftarrow E_L, E_R$ 
35            $\Sigma_L, \Sigma_R \leftarrow 0$ 
36           // IGR contribution in y,z
37           if  $\text{idir} == y$  or  $\text{idir} == z$  then
38              $\Sigma_L, \Sigma_R \leftarrow \Sigma(-2 : 3)$  along  $\text{idir}$ 
39           for  $d \leftarrow L, R$  do // Inviscid fluxes
40              $\text{rhs} \leftarrow \text{flux}(\rho_d, \mathbf{u}_d, E_d, p_d, \alpha_d, \sigma_d)$ 
41           if  $\text{idir} == x$  then
42             // IGR elliptic solve
43              $\Sigma \leftarrow \text{igr\_rhs}$ 
44             for  $d \leftarrow L, R$  do // IGR x contrib.
45                $\rho\mathbf{u}_L, \rho\mathbf{u}_R \leftarrow \rho\mathbf{u}(-2 : 3)$  along  $\text{idir}$ 
46                $\mathbf{u}_L, \mathbf{u}_R \leftarrow \rho\mathbf{u}_L, \rho\mathbf{u}_R$ 
47                $\Sigma_L, \Sigma_R \leftarrow \Sigma(-2 : 3)$  along  $\text{idir}$ 
48                $\text{rhs} \leftarrow \text{flux}(\mathbf{u}_d, \sigma_d)$ 
49    $(\rho, \rho\mathbf{u}, E, \alpha) \leftarrow (\rho, \rho\mathbf{u}, E, \alpha) + \text{dt} \cdot \text{rhs}$ 

```

the cell centers by solving the elliptic PDE (line 36) in eq. (9) and incorporated into the right-hand side (lines 34 and 41). The right-hand side of eq. (9) also requires velocity gradients, which are reused from the viscous flux calculations (lines 20 to 22).

4.3 Optimizations

Our implementation eliminates the storage of the reconstructed states (lines 23 to 29), velocity gradients (lines 16 to 20), and fluxes (lines 26, 34 and 41) and

keeps all operations in a single kernel (algorithm 1). The memory footprint is reduced by storing the intermediate variables as thread-local temporary arrays within this kernel. The algorithm only requires storing 2 copies of the conservative variables, the net flux at each grid point, and the solution and right-hand side of the elliptic PDE in eq. (9).

Each thread solves an approximate Riemann problem at the grid cell-cell interface and accumulates its contribution to the right-hand side at overlapping cells via atomic operations to prevent race conditions. During the reconstruction along the 1st coordinate dimension (x , here), the contributions to the right-hand side of the elliptic solve accumulate after computing the velocity gradients for the viscous fluxes (line 22).

The elliptic PDE is solved after the right-hand side computation is complete (line 36)*, enabling reconstruction and flux computation of the entropic pressure in the 2nd and 3rd dimensions (lines 31 to 32). The flux contribution of the entropic pressure in the first dimension is completed separately after the elliptic solve (lines 36 to 41). This structuring results in a 20-fold decrease in memory use compared to an optimized 5th-order accurate WENO+HLLC implementation in the same codebase⁴⁴.

4.4 Unified Memory

The unified memory approach uses the NVLink C2C connection on Grace-Hopper (Alps) and the Infinity-Fabric for AMD CPU-GPU connections on Frontier. This strategy is depicted in fig. 1 and uses the full capacity of the compute node, expanding beyond the GPU memory capacity without compromising performance.

4.4.1 NVIDIA approach for Alps. The compute nodes on Alps contain four NVIDIA GH200 superchips. This is a hardware-coherent system that couples a Grace CPU and a Hopper GPU using a 900 GB/s NVLink-C2C connection. This allows both processors to access all system memory at high speeds coherently and consistently. In addition to the usual CUDA allocators, GPU memory can also be allocated using system allocators such as `malloc`. The unified memory concept maps to the Grace-Hopper device and is used herein.

To realize out-of-core GPU computations, we compile and link via `-gpu=mem:unified`, instructing the compiler to use CUDA Unified Memory. This provides a single unified address space for the CPU and GPU. Our optimizations leverage this infrastructure via a *zero-copy* strategy, where the most frequently accessed data is hosted in GPU memory and the least frequent is in CPU memory. We avoid any data movement during the simulation and only perform local or remote direct accesses. This strategy eliminates the duplication of host and device buffers, maximizing simulation size. To fine-tune data placement, we provide memory hints to the CUDA driver via `cudaMemAdvise`. We use pinned allocation for buffers that stay on the CPU for the

*For typographic reasons, “right hand side” is on the left in eq. (9).

simulation lifetime. This results in a minimally intrusive out-of-core implementation that does not sacrifice GPU performance. Any potential data movement between the two physical memories is left to the CUDA driver.

The time step updates in the Runge–Kutta scheme are rearranged so only the current substep is passed to the right-hand side routine. The buffer holding the previous state is only used to update the current Runge–Kutta state. With this rearrangement, we only store one sub-step and the right-hand side buffer in GPU memory. Thus, the intermediary substep is always in CPU memory, freeing GPU memory and increasing the simulation size without sacrificing performance. The timestep updates access the Runge–Kutta substeps from their physical locations via zero-copy, simultaneously accessing data from GPU memory and CPU memory through the C2C connection.

We communicate via CUDA-aware MPI and GPUDirect, avoiding staging on host memory. We allocate the send and receive buffers on the GPU using OpenACC captures to guide MPI in selecting the GPU path.

4.4.2 AMD approach for Frontier The vendor compilers available on OLCF Frontier do not support an equivalent of unified memory for OpenACC, although both HPE’s CCE compiler and AMD’s ROCm compiler support OpenMP’s unified shared memory mode. CCE allows users to allocate device-accessible memory and request that the OpenACC runtime omit a separate device copy. The AMD heterogeneous system architecture (HSA) requires that GPU memory be accessible by the host. To reduce the memory footprint on Frontier, we thus allocate a single time-step stage as device-resident memory (`hipMalloc`) and the second as pinned host memory. We set `CRAY_ACC_USE_UNIFIED_MEM=1`, so the CCE OpenACC runtime detects that these arrays need not be mapped and uses them via zero-copy across the AMD Trento–MI250X InfinityFabric. Otherwise, the Frontier implementation follows the NVIDIA strategy, decreasing memory use on both the host and device without impacting performance. Following the NVIDIA implementation, the buffers passed to MPI are mapped to device memory by the OpenACC runtime. We therefore enable GPU-aware MPI to use the GPU buffers directly for on- and off-node communication.

4.5 Mixed precision

On GH200, we implement a mixed-precision strategy, where all computations are performed in FP32 but utilize FP16 storage. This doubles the maximum simulation size while increasing effective bandwidth. While most OpenACC constructs are readily applicable for half-precision, the NVHPC SDK does not natively support the atomic updates required by our algorithm. Instead, we implement a CUDA function called from OpenACC kernels.

5 HPC platforms and software environment

We performed calculations on OLCF Frontier and CSCS Alps. OLCF Frontier features 9,856 nodes, each with a 64-core AMD EPYC CPU and four AMD MI250X GPUs (each GPU with two GCDs and 128 GB HBM2E), delivering 1.353 EFLOP/s on HPL and a theoretical peak of 2.1 EFLOP/s, with a total memory capacity of 9.6 PB split between HBM and DDR4. CSCS Alps comprises 2,688 nodes, each with four NVIDIA Grace–Hopper GH200 superchips (10,752 total), achieving 434.9 PFLOP/s on HPL and a theoretical peak of 574.84 PFLOPs; each superchip integrates a Hopper GPU (96 GB HBM3) and a Grace CPU (72 Arm cores, 120 GB LPDDR5).

5.1 Software environment and performance baseline

We base our implementation on MFC^{7,44}, an exascale-capable compressible flow solver that ideally scales to 100% of OLCF Frontier, LLNL El Capitan, among other previous and existing flagship supercomputers^{16,32}. MFC can offload computation onto GPU devices via OpenACC and uses metaprogramming to abstract away and automate vendor-specific or burdensome optimizations. MFC has a history of being used to simulate compressible multi-species, phase, and chemically reacting fluid flows^{5,6,10,11}. We use MFC’s optimized implementation of WENO nonlinear reconstructions and HLLC approximate Riemann solves as a baseline for performance comparisons⁴⁴.

On Frontier, we use the HPE Cray Programming Environment (CCE) 24.03 release and AMD’s ROCm 6.3.1. We compile with the flags `-O3 -haggress`. On Alps we use the NVIDIA HPC SDK 25.1 and HPE Cray MPICH 8.1.30 for messaging. We compile with the flag `-gpu=fastmath`, yielding 2-4 times improvement in performance across NVIDIA architectures. Performance results are measured using a representative three-dimensional, two-fluid problem simulating the exhaust plume of a single Mach 14 jet.

5.2 Instrumentation

We measure execution time with application internal timers using Fortran standard `cpu_time` and `system_clock` procedures. On Frontier, we use HPE’s Cray Performance Analysis Tool (CrayPat) to read the Cray Power Management (PM) counters, gather the total energy consumed by the entire compute node for the time-stepping routine that aligns with the code internal timers, and divide by the number of time steps taken to find the energy per timestep. On Alps, we use `nvidia-smi` to record the module power draw and post-process the results such that we only account for power draw during time-stepping, which is then averaged and multiplied by the average time per time step. For both Frontier and Alps, we then normalize by the number of grid points to measure energy use per grid point per time step.

6 Performance results

6.1 Time step cost

Table 1 shows the normalized grind times for a two-fluid problem solved using WENO reconstructions and HLLC approximate Riemann solves with in-core computation (current state of the art, optimized implementation in MFC⁴⁴), IGR with in-core computation, and IGR with unified memory on one GH200 on Alps and one MI250X GCD on Frontier. The grind time is defined as nanoseconds per grid cell per timestep to normalize against the different problem sizes that fit within memory on the different hardware. Smaller grind times indicate shorter time to solution. Performance impacts of less than 5% are observed when moving from in-core to unified computation on the GH200 architecture. When transitioning from in-core computation to unified memory computation on Frontier, performance improvements of 20% and 42% are observed, which is a result of the non-native implementation of unified memory with OpenACC employed on Frontier. The increased grind time in calculations that utilize unified memory to increase problem size per device results from the exchange of conservative variable buffers between the CPU and GPU at each Runge-Kutta update. On both devices, the time to solution for IGR is reduced by a factor of approximately four in FP64.

Table 1. Grind time measurements for our simulations. The units are nanoseconds per grid cell per time step. We compare our baseline (WENO + HLLC in MFC) with in-core computation (current state of the art), IGR with in-core computation, and IGR with unified memory. Measurements for IGR are presented for both double (FP64) and single (FP32) precision computations. *N/A indicates baseline simulations that could not be executed due to the instability of the baseline for sub-FP64 floating point computation.

Device	Baseline	IGR (in-core)	IGR (unified)	
GH200	21.73	5.41	5.65	FP64
MI250X GCD	76.25	18.23	25.90	
GH200	*N/A	4.27	4.46	FP32
MI250X GCD	*N/A	14.60	17.61	

6.2 Scaling

Figure 4 shows the weak scaling performance on CSCS Alps and OLCF Frontier for a compressible two-fluid problem. GPU-direct MPI, unified memory, and FP32 compute and storage are used to maximize the problem size per device. A weak scaling efficiency of 98% is observed when scaling from 64 to 9.2K GH200s on Alps. On Frontier, a weak scaling efficiency of 96% is observed when scaling from 64 to 37.8K MI250X GPUs (128 to 75.6K GCDs). Unified memory and single-precision compute and storage enable a problem size of 12.2T grid cells on Alps (1098^3 per GH200) and 65T grid cells (951^3 per GCD) on Frontier.

We successfully reach *100.1T grid cells* on Frontier in the single-fluid case using 37.8K MI250X GPUs (9450 nodes), accommodating 1098^3 grid points per

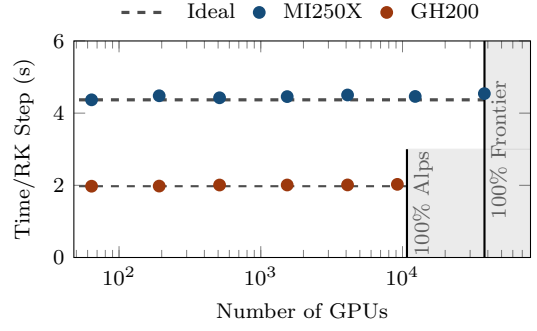


Figure 4. Weak scaling performance for a representative two-fluid problem on CSCS Alps (number of GH200s) and OLCF Frontier (number of MI250Xs). Unified memory, GPU-direct MPI, and FP32 compute and storage are used in both weak scaling runs. A weak scaling efficiency of 98% is observed when scaling from 64 to 9.2K GH200s on Alps, with a maximum problem size of 12.2T grid cells. A weak scaling efficiency of 96% is observed when scaling from 64 to 37.8K MI250X GPUs (128 to 75.6K GCDs), with a maximum problem size of 65T grid cells.

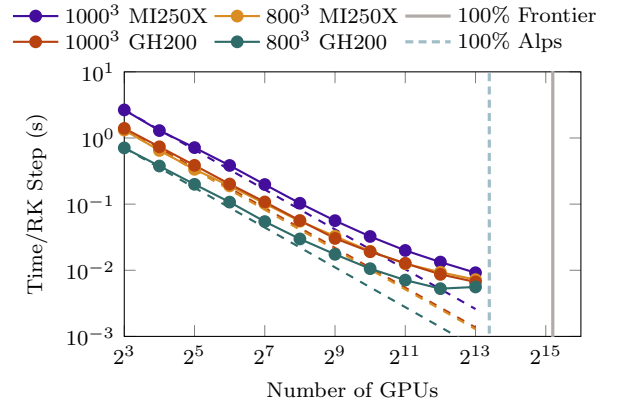


Figure 5. Strong scaling performance for a two-fluid configuration on CSCS Alps and OLCF Frontier.

GCD. On Alps, a problem size of 1611^3 is used per GH200, with FP16 storage and FP32 computation. This results in 45T grid point simulations on Alps, or 100.3T points on JSC JUPITER upon weak scaling extrapolation, despite its smaller memory capacity compared to OLCF Frontier.

Strong scaling results for a two-fluid compressible flow on Alps and Frontier are shown in fig. 5. The base case uses 8 MPI ranks arranged in a 2^3 rectilinear configuration, with each rank holding either 800^3 grid cells within device memory or 1000^3 grid cells in the unified memory case. GPU-direct MPI and single precision compute and storage are used in all runs. Strong scaling efficiencies greater than 70% are observed for a 32-fold increase in device count in both configurations and systems. Remarkably, we are able to strong scale well to nearly the entire CSCS Alps system.

6.3 Energy efficiency

Measured energy consumption per grid cell is tabulated in table 2 for a single time step of the IGR and prior-state-of-the-art WENO+HLLC implementations. The

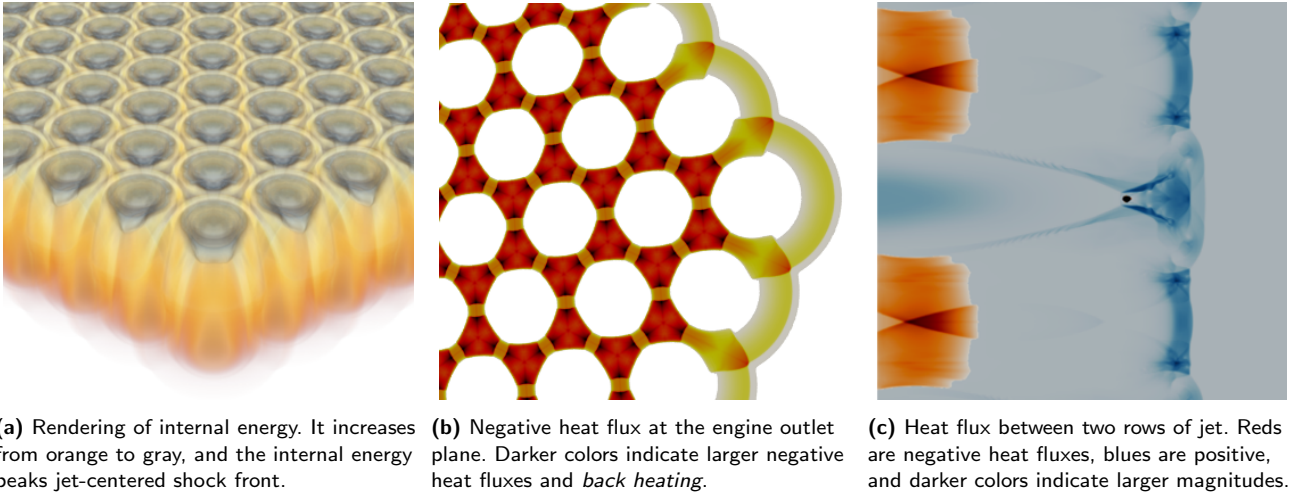


Figure 6. Simulation results near the corner of a large hexagonal array of engines with Mach 14 exhaust plumes. The very large engine array is chosen to show the ability to scale to multi-engine rockets of any conceivable size. We show that the heating encountered on the base is highly location-dependent. These results demonstrate that our approach can simulate problems at scales far exceeding that of present-day spacecraft.

Table 2. Energy results in μJ per grid cell per time step for MFC WENO against MFC IGR on a single node of Frontier and Alps. The MFC WENO+HLLC implementation is also heavily optimized for the systems benchmarked, and its performance matches current state-of-the-art implementations.

	Energy (μJ)	Frontier	Alps
Baseline (WENO + HLLC)		165.76	49.88
IGR		48.08	8.80

problem size is adjusted to exhaust the total GPU memory on a single node. Our IGR implementation shows a 3.4-times improvement in energy utilization on Frontier in the CrayPat profiled runs. For these profiled runs, the MFC internal timers reported different times than those shown in table 1 with an IGR to WENO speedup of 3.6-fold, consistent with the energy consumption. This discrepancy suggests uneven profiler overhead between the two implementations. On Alps, owing to higher power draw for WENO, we observe that energy savings exceed what is expected from pure grind time speedup, yielding a 5.7-times improvement in energy utilization.

7 Simulation results

7.1 Many-rocket configuration

Figure 6 shows visualizations of internal energy and negative heat flux for a simulation run on CSCS Alps. The simulation shows the interactions between an array of ~ 1500 Mach 14 rocket engines organized in a hexagonal grid, each resolved by 600 grid cells across its diameter. The simulation uses a Cartesian grid of 3.5 trillion (3.5T) grid cells and ran for seven hours on 9.2K GH200 superchips (2300 nodes).

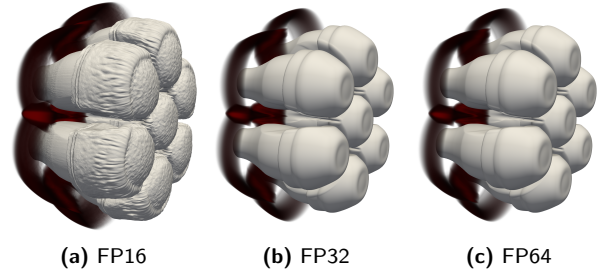


Figure 7. Simulation results showing the engine plume in white and backward heat flux in red for an array of seven engines with (a) FP16, (b) FP32, and (c) FP64 storage. FP32 and FP64 yield visually indistinguishable results. The differences in the FP16 case can arise from numerical noise, which causes a faster growth of flow instabilities and modestly larger engine plumes and backward heat flux.

7.2 Mixed precision computations

Figure 7 shows a comparison between the engine plumes and negative heat fluxes for simulations performed with FP16, FP32, and FP64 storage. Using FP16, we enable NVIDIA-based mixed-precision simulations *exceeding 100T grid points* by extrapolating our results from Alps to the upcoming JSC JUPITER, which has the same primary architecture. FP32 and FP64 yield visually identical results. We suspect that the differences in FP16 are introduced through the low-precision accumulation of numerical errors, which can trigger physical flow instabilities. In this case, it produces larger engine plumes and backward heat fluxes, although the differences appear modest.

8 Conclusion

In this work, we have provided a highly scalable code for supersonic compressible CFD and showcased its capabilities at simulating plume-plume interactions in multi-engine rockets. On the application side, this provides proof of concept that fully resolved simulations

of these systems are possible, even at scales far exceeding the sizes of present-day spacecraft. This advance paves the way for the computation-driven design of this crucial component of modern space exploration.

In terms of numerical methods, we have provided the first large-scale application of information geometric regularization (IGR). The resulting algorithmic simplifications greatly improved the efficiency of our approach, as measured by time to solution, memory cost, and power efficiency. Thus, this work demonstrates how IGR can enable state-of-the-art compressible CFD.

In terms of HPC, we have provided a prototype and proof of concept for combining unified memory and low/mixed-precision computation. The resulting computational savings enabled us to perform the first CFD simulations with more than 100 trillion grid points, exceeding current state-of-the-art by an order of magnitude while still improving the wall-time cost per grid point.

While this work focuses on one- and two-fluid (or species) cases, MFC is designed to handle more general multiphase and multicomponent flows. Our work thus has the potential to aid the numerical understanding of a wide range of physical phenomena, including reacting flows and shock-bubble interactions. We also emphasize that the IGR used in this work is entirely agnostic to the choice of discretization since it regularizes the momentum balance equation of the underlying PDE. The spatial discretizations employed in this work adhere to traditional algorithmic design patterns commonly used in compressible CFD. The removal of the need for numerical shock capturing by IGR opens up a largely unexplored design space for numerical methods for compressible and high-speed flows.

Acknowledgements

This research used resources of the Oak Ridge Leadership Computing Facility at the Oak Ridge National Laboratory (allocation CFD154, PI Bryngelson), which is supported by the Office of Science of the U.S. Department of Energy under Contract No. DE-AC05-00OR22725. This work was supported by a grant from the Swiss National Supercomputing Centre (CSCS) on Alps. FS acknowledges support from the Air Force Office of Scientific Research under award number FA9550-23-1-0668 (Information Geometric Regularization for Simulation and Optimization of Supersonic Flow).

References

- Amari Si (2016) *Information geometry and its applications*, volume 194. Springer.
- Baber WW and Ojala A (2024) Exploring emerging business model value chains in new space. In: *Space Business: Emerging Theory and Practice*. Springer Nature Singapore Singapore, pp. 169–193.
- Barter GE and Darmofal DL (2010) Shock capturing with PDE-based artificial viscosity for DGFE: Part I. Formulation. *Journal of Computational Physics* 229(5): 1810–1827.
- Bhagatwala A and Lele SK (2009) A modified artificial viscosity approach for compressible turbulence simulations. *Journal of Computational Physics* 228(14): 4965–4969.
- Bryngelson SH and Colonius T (2020) Simulation of humpback whale bubble-net feeding models. *Journal of the Acoustical Society of America* 147(2): 1126–1135.
- Bryngelson SH, Fox RO and Colonius T (2023) Conditional moment methods for polydisperse cavitating flows. *Journal of Computational Physics* 477: 111917.
- Bryngelson SH, Schmidmayer K, Coralic V, Meng JC, Maeda K and Colonius T (2021) MFC: An open-source high-order multi-component, multi-phase, and multi-scale compressible flow solver. *Computer Physics Communications* 266: 107396.
- Cao R and Schäfer F (2023) Information geometric regularization of the barotropic Euler equation. *arXiv preprint arXiv:2308.14127*.
- Cao R and Schäfer F (2024) Information geometric regularization of unidimensional pressureless Euler equations yields global strong solutions. *arXiv preprint arXiv:2411.15121*.
- Charalampopoulos A, Bryngelson SH, Colonius T and Sapsis TP (2022) Hybrid quadrature moment method for accurate and stable representation of non-Gaussian processes and their dynamics. *Philosophical Transactions of the Royal Society A* 380(2229).
- Cisneros-Garibay E, Le Berre H, Bryngelson SH and Freund JB (2025) Pyrometheus: Symbolic abstractions for XPU and automatically differentiated computation of combustion kinetics and thermodynamics. *arXiv preprint arXiv:2503.24286*.
- Cook AW and Cabot WH (2004) A high-wavenumber viscosity for high-resolution numerical methods. *Journal of Computational Physics* 195(2): 594–601.
- Coralic V and Colonius T (2014) Finite-volume WENO scheme for viscous compressible multicomponent flows. *Journal of Computational Physics* 274: 95–121.
- Denis G, Alary D, Pasco X, Pisot N, Texier D and Toulza S (2020) From new space to big space: How commercial space dream is becoming a reality. *Acta Astronautica* 166: 431–443.
- Dongarra J, Gunnels J, Bayraktar H, Haidar A and Ernst D (2024) Hardware trends impacting floating-point computations in scientific applications. *arXiv preprint arXiv:2411.12090*.
- Elwasif W, Bastrakov S, Bryngelson SH, Bussmann M, Chandrasekaran S, Ciorba F, Clark MA, Debus A, Godoy W, Hagerty N, Hammond J, Hardy D, Harris JA, Hernandez O, Joo B, Keller S, Kent P, Le Berre H, Lebrun-Grandie D, MacCarthy E, Vergara VGM, Messer B, Miller R, Oral S, Piccinalli JG, Radhakrishnan A, Simsek O, Spiga F, Steiniger K, Stephan J, Stone JE, Trott C, Widera R and Young J (2023) Early application experiences on a modern GPU-accelerated Arm-based HPC platform. In: *HPC Asia '23*, International Workshop on Arm-based HPC: Practice and Experience (IWAHPCE). Singapore, pp. 35–49.
- Gottlieb S and Shu CW (1998) Total variation diminishing Runge–Kutta schemes. *Mathematics of Computation* 67(221): 73–85.

18. Guermond JL, Pasquetti R and Popov B (2011) Entropy viscosity method for nonlinear conservation laws. *Journal of Computational Physics* 230(11): 4248–4267.
19. Guermond JL and Popov B (2014) Viscous regularization of the Euler equations and entropy principles. *SIAM Journal on Applied Mathematics* 74(2): 284–305.
20. Haidar A, Bayraktar H, Tomov S, Dongarra J and Higham NJ (2020) Mixed-precision iterative refinement using tensor cores on GPUs to accelerate solution of linear systems. *Proceedings of the Royal Society A* 476(2243): 20200110.
21. Harten A, Engquist B, Osher S and Chakravarthy SR (1997) Uniformly high order accurate essentially non-oscillatory schemes, III. *Journal of Computational Physics* 131(1): 3–47.
22. Harten A, Lax PD and Leer Bv (1983) On upstream differencing and Godunov-type schemes for hyperbolic conservation laws. *SIAM Review* 25(1): 35–61.
23. Kawai S, Shankar SK and Lele SK (2010) Assessment of localized artificial diffusivity scheme for large-eddy simulation of compressible turbulent flows. *Journal of Computational Physics* 229(5): 1739–1762.
24. Kuzmin D (2020) Monolithic convex limiting for continuous finite element discretizations of hyperbolic conservation laws. *Computer Methods in Applied Mechanics and Engineering* 361: 112804.
25. Laboratory IC (2023) HPL-MxP mixed-precision benchmark. URL <https://hpl-mxp.org>.
26. Lehmann M, Krause MJ, Amati G, Sega M, Harting J and Gekle S (2022) Accuracy and performance of the lattice Boltzmann method with 64-bit, 32-bit, and customized 16-bit number formats. *Physical Review E* 106(1): 015308.
27. Liu XD, Osher S and Chan T (1994) Weighted essentially non-oscillatory schemes. *Journal of Computational Physics* 115(1): 200–212.
28. Mani A, Larsson J and Moin P (2009) Suitability of artificial bulk viscosity for large-eddy simulation of turbulent flows with shocks. *Journal of Computational Physics* 228(19): 7368–7374.
29. Mehta M, Canabal F, Tashakkor SB and Smith SD (2013) Numerical base heating sensitivity study for a four-rocket engine core configuration. *Journal of Spacecraft and Rockets* 50(3): 509–526.
30. Pekkanen SM (2019) Governing the new space race. *AJIL Unbound* 113: 92–97.
31. Persson PO and Peraire J (2006) Sub-cell shock capturing for discontinuous Galerkin methods. In: *44th AIAA Aerospace Sciences Meeting and Exhibit*. p. 112.
32. Radhakrishnan A, Le Berre H, Wilfong B, Spratt JS, Rodriguez Jr M, Colonius T and Bryngelson SH (2024) Method for portable, scalable, and performant GPU-accelerated simulation of multiphase compressible flow. *Computer Physics Communications* 302: 109238.
33. Ren F (2024) Numerical-study of large-liquid rocket plume-flow-field. In: *Journal of Physics: Conference Series*, volume 2755. IOP Publishing, p. 012038.
34. Roe PL (1981) Approximate Riemann solvers, parameter vectors, and difference schemes. *Journal of Computational Physics* 43(2): 357–372.
35. Rossinelli D, Hejazialhosseini B, Hadjidoukas P, Bekas C, Curioni A, Bertsch A, Futral S, Schmidt SJ, Adams NA and Koumoutsakos P (2013) 11 PFLOP/s simulations of cloud cavitation collapse. In: *Proceedings of the International Conference on High Performance Computing, Networking, Storage and Analysis*. pp. 1–13.
36. Rueda-Ramírez AM, Pazner W and Gassner GJ (2022) Subcell limiting strategies for discontinuous Galerkin spectral element methods. *Computers & Fluids* 247: 105627.
37. Sathyanarayana S, Bernardini M, Modesti D, Pirozzoli S and Salvadore F (2025) High-speed turbulent flows towards the exascale: STREAMS-2 porting and performance. *Journal of Parallel and Distributed Computing* 196: 104993.
38. Shu CW (1998) Advanced numerical approximation of nonlinear hyperbolic equations, chapter essentially non-oscillatory and weighted essentially non-oscillatory schemes for hyperbolic conservation laws.
39. Toro EF (2013) *Riemann solvers and numerical methods for fluid dynamics: A practical introduction*. Springer Science & Business Media.
40. Toro EF (2019) The HLLC riemann solver. *Shock Waves* 29(8): 1065–1082.
41. Van Leer B (1979) Towards the ultimate conservative difference scheme. V. a second-order sequel to godunov’s method. *Journal of Computational Physics* 32(1): 101–136.
42. Wang X, Xu X and Yang Q (2022) Base thermal environment on multinozzle rocket configurations. *Journal of Spacecraft and Rockets* 59(6): 1966–1975.
43. Wang X, Xu X, Yu J and Yang Q (2024) Effect of free-stream Mach number on the base thermal environment of launch vehicle. *Journal of Thermal Science* 33(6): 2426–2436.
44. Wilfong B, Le Berre H, Radhakrishnan A, Gupta A, Vaca-Revelo D, Adam D, Yu H, Lee H, Chreim JR, Carcana Barbosa M, Zhang Y, Cisneros-Garibay E, Gnanaskandan A, Rodriguez Jr M, Budiardja RD, Abbott S, Colonius T and Bryngelson SH (2025) MFC 5.0: An exascale many-physics flow solver. *arXiv preprint arXiv:2503.07953*.
45. Yeung P, Ravikumar K, Nichols S and Uma-Vaideswaran R (2025) GPU-enabled extreme-scale turbulence simulations: Fourier pseudo-spectral algorithms at the exascale using OpenMP offloading. *Computer Physics Communications* 306: 109364.